

FEATURE ARTICLE

Coherently Controlled Ultrafast Four-Wave Mixing Spectroscopy

Joshua C. Vaughan,[†] T. Hornung, K. W. Stone, and Keith A. Nelson**Department of Chemistry, Massachusetts Institute of Technology, Cambridge, Massachusetts 02139**Received: September 25, 2006; In Final Form: February 7, 2007*

A novel approach to coherent nonlinear optical spectroscopy based on two-dimensional femtosecond pulse shaping is introduced. Multiple phase-stable output beams are created and overlapped at the sample in a phase-matched boxcars geometry via two-dimensional femtosecond pulse shaping. The pulse timing, shape, phase, and spectral content within all beams may be specified, yielding an unprecedented level of control over the interacting fields in nonlinear spectroscopic experiments. Heterodyne detection and phase cycling of the nonlinear signal are easily implemented due to the excellent phase stability among all output beams. This approach combines the waveform generation capabilities of magnetic resonance spectroscopy with the wavevector specification and phase matching of nonlinear optical spectroscopy, yielding the control capabilities and signal selectivity of both. Results on four prototype systems are used to illustrate some of the novel possibilities of this method.

I. Introduction

Nonlinear multidimensional spectroscopy provides a means to disentangle signal contributions hidden within broad line-shapes, revealing molecular structure, vibrational and electronic motions, interactions, and relaxation processes. This is especially the case for condensed phase measurements in which complex inter- or intramolecular interactions, possibly occurring over a wide range of time scales, as well as environmental heterogeneity that may be static or slowly varying, may be obscured within the broad spectral features of linear absorption measurements. Nonlinear multidimensional spectroscopic methods may permit spreading of congested spectra along multiple time or frequency coordinates, as in nuclear magnetic resonance (NMR) spectroscopy,¹ thereby enabling quantitative determination of couplings, anharmonicities, relative dipole orientations, and dynamical processes that depend on them. These unique abilities have been elegantly demonstrated in many experiments over the past several years using coherent two-dimensional (2D) spectroscopy with ultrashort pulses in the mid-infrared^{2–9} and in the visible or near-infrared^{10–15} spectral ranges.

An important requirement for coherent 2D spectroscopy is that the nonlinear signal be detected interferometrically, permitting characterization of the full signal field. This requires phase stability of the setup on the order of a fraction of the wavelength of the interacting pulses. In the infrared portion of the spectrum, robust mechanical components within a sealed box can be used to minimize phase variations among the multiple beams, but the problem is exacerbated substantially when using shorter wavelengths in the visible and near-IR spectral regions.¹⁰ This is the primary reason that progress has been faster in 2D vibrational spectroscopy than in its electronic analogs.

The other key requirement for coherent nonlinear spectroscopy is phase matching, which is achieved through proper adjustment of the wavevectors of the multiple incident beams. A collinear geometry¹² naturally provides both phase matching (in all orders of the nonlinearity for degenerate signals) and phase stability, because all the interacting pulses travel the same optical path. Pulse shaping with an acousto-optic modulator has been used in this manner to control the incident field components, i.e., the relative delays and phases of various incident pulses, and to extract the nonlinear signal of interest by phase cycling. However, in a collinear geometry the nonlinear signal of interest must be detected against a background that is many orders of magnitude more intense because it includes the incident

* Corresponding author. E-mail: kanelson@mit.edu.

[†] Present address: Department of Chemistry and Chemical Biology, Harvard University, Cambridge, Massachusetts and Howard Hughes Medical Institute, Cambridge, Massachusetts 01238.



Joshua C. Vaughan was born in San Mateo, CA, in 1976. He received a B.A. in chemistry from Reed College in 2000 and a Ph.D. in physical chemistry from MIT in 2005. For his graduate research, he developed methods for two-dimensional femtosecond pulse-shaping, which he then applied to the coherent control of lattice excitations in crystalline solids and to ultrafast multidimensional spectroscopy. He is currently a postdoctoral associate in the lab of Xiaowei Zhuang at Harvard University.



Thomas Hornung studied physics at the TH Darmstadt and TU Munich in Germany and received his Ph.D. degree in 2002. Since 1999 he has been conducting research in the field of coherent control and nonlinear spectroscopy at the Max-Planck Institute of Quantum Optics. In 2003 he joined the group of Keith Nelson at MIT as a postdoctoral scholar, where he experienced the most enjoyable research time of his career. The work of this time includes the development of a pulse shaping based nonlinear spectroscopy device and trying to reach the nonlinear regime with high amplitude terahertz pulses. Now he is working as product manager at Carl Zeiss SMT AG in Oberkochen/Germany.

light fields as well as all other nonlinear responses. Therefore, approaches using a non-collinear beam arrangement, where the signal emerges from the sample at a different wavevector than the input beams, are favored. In this case, however, phase stability has only been accomplished through active stabilization with multiple interferometers¹⁵ or through the use of diffractive optics¹⁶ to create multiple beams that traverse a common set of optical elements.^{13,17} In the latter arrangement, pulse delays have been controlled with refractive optical elements, i.e., glass wedges with variable thicknesses inserted into the beam paths. However, as with a conventional delay line, this shifts both the envelopes and phases of the beams, requiring delay steps much smaller than the optical wavelength and, for each step, interferometric determination of the phase.

In addition to interferometric stability and phase matching, waveform shaping capabilities are extremely important for the most versatile implementations of coherent multidimensional spectroscopy. In NMR, sophisticated radio frequency pulse



Katherine Walowicz Stone was born in Sterling Heights, MI. She received her B.S. in chemistry and chemical engineering from Michigan State University in 2003. She is currently pursuing her doctoral degree in physical chemistry at MIT under the guidance of Dr. Keith A. Nelson. Her future research interests include adapting spatiotemporal pulse-shaping for 2D FT spectroscopy in the UV and continuing her work on many-body dynamics in semiconductor quantum wells.



Keith A. Nelson is a professor of chemistry at MIT. He received his B.S. and Ph.D. degrees at Stanford University in 1976 and 1981, respectively, and was a postdoctoral scholar at UCLA before joining the MIT faculty in 1982. His research includes ultrafast spectroscopy of condensed phase structural and chemical rearrangements and the collective degrees of freedom that mediate them. Recent work includes the development of terahertz and optical pulse-shaping methods that enable coherent spectroscopy and control of collective modes including acoustic phonons, optic phonons and phonon-polaritons, and excitons.

sequences with specified time-dependent amplitude and phase profiles provide the foundation upon which modern multidimensional methods are based. As mentioned above, femtosecond pulse shaping has been used for coherent multidimensional optical spectroscopy in a collinear geometry, but in the otherwise advantageous non-collinear arrangement, in which distinct beams are generated with partial reflectors or with diffractive elements, a pulse shaper would be needed in each of the beams to provide general waveform shaping capabilities. This would introduce substantial additional complexity into an already challenging experimental operation.

In this Feature Article we discuss a new approach to 2D (or generally, multidimensional) optical spectroscopy that is based on 2D femtosecond pulse shaping.^{18–20} This approach yields interferometric phase stability, phase matching in a noncollinear geometry, and generalized waveform shaping capabilities in each incident beam. The facile arrangement is remarkably robust, involving no partially reflecting or diffracting beamsplitters, no interferometric feedback loops, no mechanical or refractive delay stages, and indeed no active optical elements of any kind other

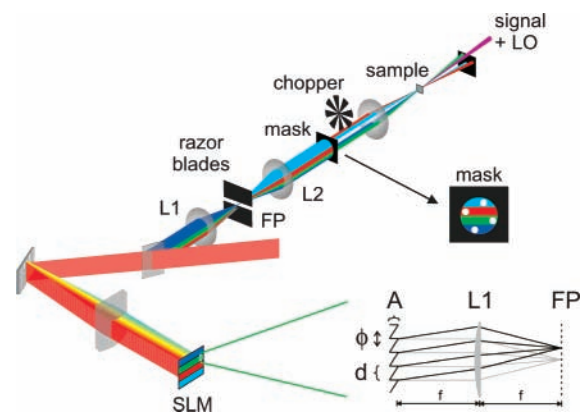


Figure 1. Experimental apparatus for degenerate four-wave mixing spectroscopy based on two-dimensional femtosecond pulse shaping. The figure shows every optical element up to the sample except for a neutral density filter in the LO beam and a glass plate of equal thickness in the other beams. Signal is measured with a single-element photodetector or, for spectral interferometry, with a spectrometer and CCD element.

than the 2D pulse shaper—and rather few optical elements altogether. In many respects, this approach rescues what has been to date a rocky marriage between multidimensional NMR methodologies and coherent optical spectroscopy. It offers the prospect of coherent multidimensional optical spectroscopy to a far broader user community than the current handful of specialized research groups worldwide, with far greater capabilities including waveform shaping, phase cycling, rotating frame detection, and others that are familiar from magnetic resonance.

We begin with a description of the experimental apparatus and its capabilities. Next, we present results on four prototype systems, liquid diiodomethane, atomic rubidium vapor, potassium dimer vapor, and semiconductor quantum wells. In each section we also assess the prospects for future developments and applications.

II. Experimental Section

Figure 1 shows the optical apparatus used for the experiments reported here. The active component of the experiment is a 2D pulse shaper configured for diffraction-based pulse shaping, discussed in detail elsewhere.^{20,21} The 40 fs input laser pulses centered at 800 nm are spectrally dispersed with a grating and cylindrical lens pair onto a 2D liquid crystal spatial light modulator (LC SLM). The beam at the 2D LC SLM is divided into four horizontal stripes, denoted by dark blue, green, red, and light blue. Three of the output pulses are used to generate the nonlinear signal whose field may be characterized through heterodyne mixing with the fourth (local oscillator) output. Within each of the horizontal regions, a series of vertical sawtooth phase functions is used to diffract a specified amount of the different spectral components into a first-order direction. The amplitude A of the sawtooth phase function determines the amplitude of the diffracted light, and the spatial phase ϕ controls the phase of the diffracted light, as shown in the inset of Figure 1. By controlling the phase and amplitude of the diffracted spectral components, the full properties of the laser field may be specified. For instance, the application of a linear spectral phase variation as a function of frequency in one of the SLM stripes executed through a linear variation of the sawtooth spatial phase as a function of horizontal position will shift the corresponding pulse in time, whereas a cosinusoidal spectral amplitude modulation will create a double pulse, etc. This pulse shaping with sawtooth phase functions is performed indepen-

dently for each of the four horizontal regions of the input laser beam. A pair of razor blades is situated at the focal plane (FP) of lens L1 to block all but the first-order diffracted light.

Notice that after lens L2 collimates the laser beam, the four shaped outputs propagate coplanar with respect to each other, one above the other. To phase match this coplanar geometry for degenerate four-wave mixing, relatively small angles must be used.²² This reduces the ability to perform background-free measurements, especially for weakly emitting samples. In contrast, a folded-forward BOXCAR geometry, where the beams are arranged on the corners of a square, optimally fulfills phase matching for degenerate or near-degenerate measurements, yielding a larger signal intensity and better discrimination against unwanted contributions. To configure the apparatus for this BOXCAR geometry, a spatial mask with four 2 mm diameter holes on the vertices of an imaginary square with 7 mm long edges was used to carefully mask each of the horizontal regions of the shaped laser beam. The imaginary square defined by the four holes of the mask was rotated by about 25 degrees from vertical such that each of the four holes of the mask was positioned within a different horizontal slice of the beam. The four transmitted regions of each of the horizontal slices were thus arranged in the BOXCAR geometry. Three of the output regions (illustrated in Figure 1 as red, green, and light blue) constituted the three input fields used to generate the nonlinear signal in our measurements. The dark blue region was used for a reference local oscillator (LO) beam. In some cases, interferometric detection was not employed and the LO beam was blocked at the position of the spatial mask.

After the spatial mask, the four beams were focused to a common point within the sample by a 15 cm lens. All transmitted beams were then blocked except for the signal beam and, if it was not blocked at the mask plane, the LO beam. When the LO beam was used, it was necessary to attenuate it because the nonlinear signals are generally quite weak and would otherwise be overwhelmed by the LO. Although in principle it is possible to attenuate the LO by reducing the amplitude A of the corresponding stripe of the vertical sawtooth phase function applied on the LC SLM, the quality of the shaped pulses is degraded at very low amplitudes. Therefore, we chose to attenuate the LO with a neutral density filter placed in the path of the LO beam before the sample. When doing so, it was important to use a filter with good parallelism such that the transmitted beam was not refracted in a direction away from the detector. In addition, a glass plate of equal thickness and good parallelism was introduced in the other three beams to compensate for the additional temporal delay. The signals were measured with either a photodiode or a spectrometer. When a photodiode was used, one of the three input beams was chopped at half the repetition rate of the laser to allow for lock-in detection.

A tremendous benefit of the apparatus is that all beams propagate through the same set of optics, such that the relative path length traversed by all beams is interferometrically stable. This property greatly facilitates the coherent characterization of the emitted signal field, required for most 2D spectroscopic methods, because the signal field is analyzed through measurement of the interference fringes between it and the copropagating LO reference field within a spectrometer. Small path length variations on the order of the wavelength of the laser pulses cause the interference fringes between the signal and LO to shift significantly, introducing crippling distortions in the measured signals. The common path geometry used here makes the apparatus rather insensitive to vibrations in the mounts and

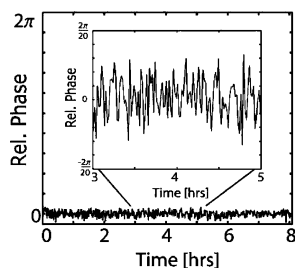


Figure 2. Measurement of the phase stability between a nonlinear signal from Rb atoms and the LO over 8 h, indicating a root-mean-square phase stability of $\lambda_o/67$.

holders for each optic. Only relatively high-order vibrational modes, for instance the “warping” of a mirror or lens, or turbulence in the air, are capable of introducing phase shifts between the beams. Stability measurements between a nonlinear signal and the LO are shown in Figure 2. The rms stability over 8 h is only 1.5%, or $\lambda_o/67$, even though no efforts were made to use especially sturdy optical mounts and even though the apparatus was not contained within a box to minimize phase shifts due to air currents.

The range of delay times accessible by the pulse shaper is approximately ± 4 ps when using ≈ 40 fs laser pulses. The ratio of pulse delay to pulse duration in femtosecond pulse shaping is primarily a function of the number of pixels of the spatial light modulator.²³ If a LC SLM with twice as many pixels were used, the pulse delay range would approach ± 8 ps for the same input pulse duration. Alternatively, if 120 fs pulses were used with the present device, the delay range could be extended to approximately ± 12 ps with the proper choice of grating and cylindrical lens to optimally disperse the laser spectrum. It should be noted that the amplitude of delayed pulses gradually decreases as the pulses are shifted away from time zero due to the finite pixel size and spectral resolution of the pulse shaping apparatus.²⁴ If desired, amplitude shaping of the output pulse could be used to compensate for the natural rolloff of the pulse as it is delayed or advanced from time zero. Instead, the rolloff may be accounted for in the data analysis by either characterizing the rolloff prior to the experiment or by recording the intensity of the pulse for all delays during a measurement.

One drawback of the apparatus is that much of the input laser energy is wasted. Fortunately, the experiments reported here did not suffer from the low efficiency of the apparatus because there was an abundance of energy provided by our laser source—a 1 kHz amplified Ti:sapphire laser, with 1.5 mJ pulses of 40 fs duration and a center wavelength of 800 nm. The losses arise from both the diffraction-based pulse shaping apparatus, which is about 20% efficient, and the spatial mask, which is about 5% efficient. In the pulse shaping portion of the apparatus, most of the losses arise from two passes through a 50% beamsplitter. The 1200 lp/mm holographic grating is itself 90% efficient per pass. On previous occasions, we have used the pulse shaper with the LC SLM slightly tilted such that the reflected, modulated beam was sent out of the system at a small angle relative to the input and could be picked off with a mirror. The efficiency of this pulse shaping arrangement is about 80% and the fidelity of the shaped waveforms is still excellent. Methods to improve the efficiency of the spatial masking process, such as the use of multiple-lens arrays, are currently under consideration.

III. Results and Discussion

As with any new method, a first objective is to generate results from systems that are well understood so that the method

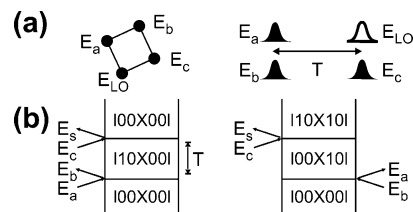


Figure 3. (a) Beam geometry (left) and pulse sequence (right) for nonresonant transient grating measurements. (b) Contributing Feynman diagrams for a given vibrational mode.

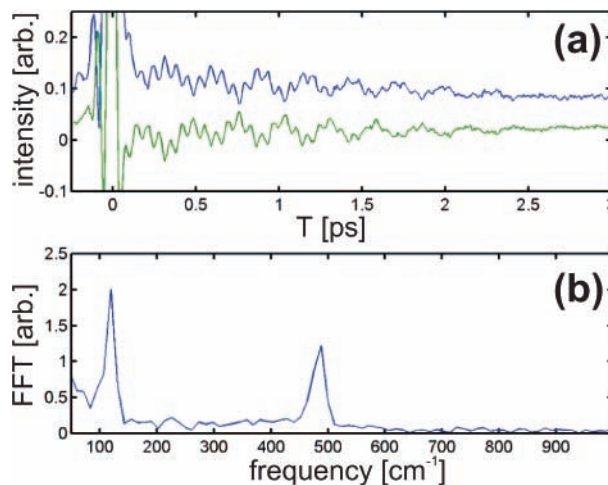


Figure 4. (a) Heterodyne-detected transient grating signals with (green, bottom) and without (blue, top) one of the input beam phases flipped by π . Signals are shifted vertically for clarity. (b) Fourier transform of blue signal in (a), indicating the expected vibrational modes.

itself can be tested thoroughly. To that end, the first experiments discussed are heterodyne-detected transient grating measurements of liquid diiodomethane, a system that is Raman active and does not possess electronic resonances within our laser bandwidth. Single- and multiple-pulse excitation are used to generate and manipulate vibrational wavepackets in the ground electronic state via impulsive stimulated Raman scattering. Next, one- and two-dimensional DFWM measurements of atomic rubidium vapor are described. Some of the versatility of the apparatus is demonstrated with measurements conducted in a hybrid time–frequency domain (delayed pulse in one input beam, and spectral manipulation of the other beams) and in the frequency domain (via spectral filtering of the input beams). After that, we present DFWM measurements on potassium dimer molecules in the gas phase, with different pulse sequences that exert a strong influence on the system response. We also demonstrate versatile phase-cycling methods borrowed from multidimensional NMR, which allow for the isolation of the nonlinear signal of interest in the presence of competing signals that would otherwise seriously degrade the measurements. Finally, we report preliminary coherent 2D spectroscopic measurements of a GaAs/AlGaAs multiple quantum well structure.

A. Transient Grating Measurements on Diiodomethane.

Two Raman-active vibrational modes of diiodomethane have periods that exceed our laser pulse duration, the C–I symmetric stretch at 488 cm^{-1} (68.3 fs period) and an I–C–I bending mode at 123 cm^{-1} (271 fs period). These vibrational modes may be excited through impulsive stimulated Raman scattering (ISRS)^{25,26} as part of a DFWM measurement. The beam geometry for all measurements in this article is shown in Figure 3a. Input fields E_a , E_b , and E_c generate a nonlinear signal field E_s in the direction given by wavevector $\vec{k}_s = \vec{k}_a - \vec{k}_b + \vec{k}_c$. The

pulse configuration used for heterodyne-detected nonresonant transient grating measurements is shown in Figure 3a. Fields E_a and E_b excite coherent vibrational motion through ISRS, which is then probed after a time T by pulse E_c . The local-oscillator pulse E_{LO} is scanned in time synchronously with E_c to enable heterodyne detection of the signal.^{16,27} Because there are no resonant transitions in diiodomethane that occur within the spectral bandwidth of our laser, pairs of light-matter interactions occur simultaneously, as shown in the two Feynman diagrams²⁸ in Figure 3b. For a system with two oscillators, m and n , initially in the ground vibrational states, the signal field E_s expected when using delta-like input pulses is

$$E_s(T) \propto \Theta(T) \{ K_m \exp[-\Gamma_m T] \sin(\omega_m T) + K_n \exp[-\Gamma_n T] \sin(\omega_n T) \} \quad (1)$$

where Θ is a Heaviside step function, K describes the relative contribution of a given vibrational mode to the signal and is determined by the differential polarizabilities, Γ is the dephasing rate, and ω is the frequency of the vibrational mode. The diagrammatic representation²⁸ of the above equation is shown in Figure 3b for the vibrational mode m .

Figure 4a shows the nonresonant transient grating signal for diiodomethane in a 1 mm path length cuvette at room temperature, consisting of both slow and fast oscillatory components, as well as a large nonresonant electronic response at time zero (not described in eq 1). The frequencies of the fast and slow oscillations agree with the expected values, shown in the Fourier transform in (b). When the phase of one of the input beams (in this case, beam E_a) is flipped by π with the pulse shaper, the measured signal becomes inverted, as shown in the green (bottom) curve in (a). This inversion is a result of phase-sensitive detection of the signal. The heterodyne-detected signal intensity $I_{\text{det}}(T)$ is given by

$$I_{\text{det}}(T) \propto |E_s(T)|^2 + |E_{LO}(T)|^2 + 2|E_s(T)||E_{LO}(T)| \cos(\Delta\phi) \approx |E_{LO}(T)|^2 + 2|E_s(T)||E_{LO}(T)| \cos(\Delta\phi) \quad (2)$$

where the approximation holds true for signals $E_s(T)$ that are much weaker than the reference pulse $E_{LO}(T)$, and where $\Delta\phi$ here represents the phase difference between E_s and E_{LO} . When $\Delta\phi$ shifts by π , the signal relative to E_{LO} becomes inverted. Through chopping of beam E_c and lock-in detection, the signal that would have otherwise resulted from $|E_{LO}(T)|^2$ was effectively subtracted off.

A second set of transient grating measurements is shown in Figure 5. This time, the pulse shaping capabilities were used to produce a pair of output pulses for each of beams E_a and E_b with a variable interpulse separation, Δ , as shown in (a). When Δ matches a vibrational period, i.e., $\Delta = n(2\pi/\omega)$, the vibrational response is driven in phase and amplified, but if $\Delta = (n + 1/2)(2\pi/\omega)$ then the vibrational response is driven out of phase and is suppressed.^{29,30} Note that the second pulse within each pulse pair was fixed at time zero (i.e., unshifted by the pulse shaper relative to the incident pulse) and the first pulse was shifted in time to precede the second pulse by Δ . Transient grating measurements were performed for many different values of the interpulse separation. The full two-dimensional data set is shown in (b). Thick black lines in the shape of the letter V indicate the nonresonant electronic responses (saturating the colormap) that appear when the probe pulse E_c is temporally overlapped with either pair of excitation pulses. The rest of the data show that the two vibrational modes are enhanced or suppressed as expected. For instance, when $\Delta = 0.27$ ps or 0.41

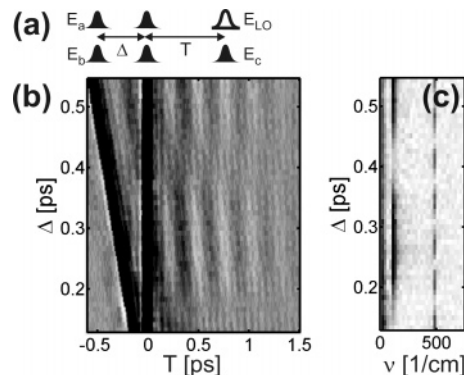


Figure 5. (a) Double-pulse excitation scheme. (b) Transient grating data from CH_2I_2 liquid recorded as a function of interpulse delay Δ and probe delay T . (c) Fourier transform of (b) for different values of Δ .

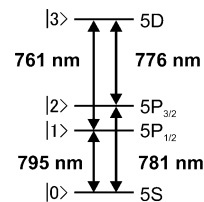


Figure 6. Energy level system for gas phase Rb atoms and corresponding transition wavelengths.

ps, either 1 or 1.5 times the bending mode period, respectively, the slower oscillatory signal is either amplified or not observed. Periodic enhancement and suppression may also be observed for the C–I stretching mode at intervals of 68 fs in the value of Δ . The measured signals contain either fast or slow oscillatory components, as can be clearly seen in the Fourier transform of the full data set for all values of Δ , shown in (c), where either vibrational mode may be suppressed or enhanced (peaks near 120 and 500 cm^{-1}) depending upon the interpulse delay.

From the transient grating measurements shown in this section, it is clear that the DFWM apparatus based on 2D pulse shaping may be used for sophisticated nonlinear optical measurements requiring interferometric phase stability (for heterodyne detection) and precise delays between pairs of incident pulses. All pulse delays, phase modulations, and pulse shapes (i.e., multiple pulse waveforms) were created by varying the patterns on the computer-controlled LC SLM. Multiple-pulse excitation is easily implemented and can help to simplify the system response. Furthermore, the ability to manipulate the phase of the signal beam by modulating the relative phases of the input pulses foreshadows the phase-cycling methods that will be used in later sections to eliminate spurious signals that are not dependent upon all input beams. However, the CH_2I_2 vibrational response itself is not sensitive to the optical phases because it is driven by ISRS, a second-order process. In the next sections we examine systems that have absorption resonances at the laser wavelengths, and whose electronic responses therefore depend on the optical phases of the various fields.

B. DFWM Measurements on Atomic Rubidium Vapor.

Atomic rubidium vapor possesses four electronic resonances in the vicinity of the Ti:sapphire laser bandwidth (~ 800 nm), as shown in Figure 6. In the Feynman diagrams used within this section, we will refer to the four relevant electronic levels (5S, $5P_{1/2}$, $5P_{3/2}$, and 5D) of rubidium as $|0\rangle$, $|1\rangle$, $|2\rangle$, and $|3\rangle$, respectively. All but the 761 nm resonance are accessible by our laser. The rubidium sample cell (Triad Technology Inc.) consists of a 2 in. path length sealed quartz cell containing 20

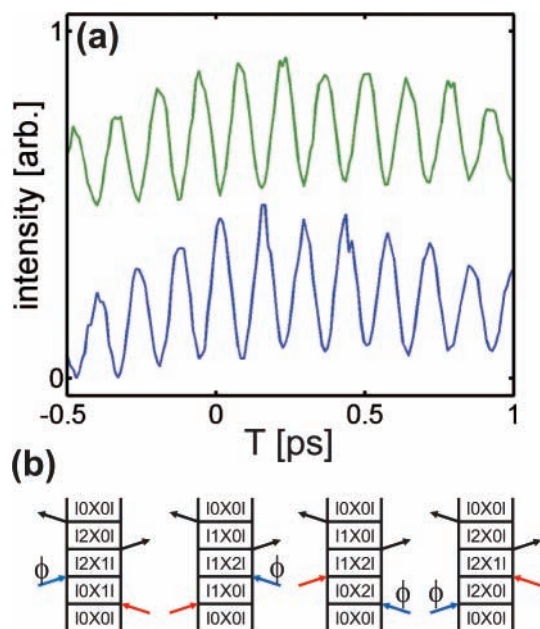


Figure 7. Hybrid time–frequency domain DFWM measurements in rubidium vapor. Phase-shifting of the “blue” spectral components of E_a and E_b by π results in a π phase shift of the measured transient (green curve). (b) Relevant Feynman diagrams for positive time delay T , where the phase ϕ is zero for the blue curve in (a) or π for the green curve in (a). There are also four diagrams for negative T .

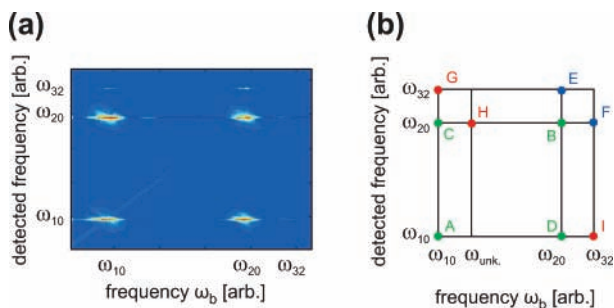


Figure 8. Two-dimensional frequency-domain spectrum of Rb plotted on a logarithmic scale. The y-axis represents the detection frequency of the spectrometer, and the x-axis represents the excitation frequency of the conjugate field, labeled here as ω_b . (a) Measured 2D spectrum. The faint line along the diagonal is due to light scattered from E_b as it was being scanned. (b) Schematic illustration labeling various peak positions. Green and blue circles represent the expected peaks. Red circles represent additional peaks observed in the experiment, possibly due to effects out of the third-order perturbative limit.

mTorr of helium buffer gas in addition to a small amount of rubidium. The cell was heated to approximately 130 °C.

Our first DFWM measurement on atomic rubidium vapor constitutes a mixed time–frequency domain measurement. Fields E_a and E_b were each shaped identically such that their spectral amplitude consisted of two fairly narrow frequency bands centered at the two 5S–5P transition frequencies. The resulting pulses had a duration of 0.7 ps and were time-coincident. Because the two frequency bands originate from a common coherent pulse spectrum, they and the resonant electronic responses induced by them oscillate with a well-defined phase relationship, resulting in a coherence or wavepacket in the 5P levels with a beat period of 147 fs, given by the 5P level splitting. An unshaped, 40 fs pulse (E_c) was variably delayed to probe this coherence, and the time-integrated signal (with no LO field) was measured with a photodiode. The observed oscillatory signal shown in Figure 7a is described by

TABLE 1: Peak Labels for 2D Rubidium Spectrum in Figure 8 and Corresponding Feynman Diagrams Described in the Appendix (Figure 17)^a

peak label	corresponding diagrams
A	$R_5(1,1)$, $R_6(1,1)$, $R_7(1,1)$, $R_8(1,1)$
B	$R_5(2,2)$, $R_6(2,2)$, $R_7(2,2)$, $R_8(2,2)$
C	$R_5(1,2)$, $R_6(1,2)$, $R_7(1,2)$, $R_8(1,2)$
D	$R_5(2,1)$, $R_6(2,1)$, $R_7(2,1)$, $R_8(2,1)$
E	$R_2(2,1 \text{ or } 2)$, $R_3(2,1 \text{ or } 2)$, $R_4(2,1 \text{ or } 2)$
F	$R_1(2,1 \text{ or } 2)$
G–I	not assigned

^a A total of 24 diagrams contribute to the assignment of the peaks observed in the 2D data of Figure 8.

the four Feynman diagrams shown in (b) that reveal coherence between the two 5P levels ($|1\rangle$ and $|2\rangle$) during T . Additional diagrams (not shown) produce signals that evolve in populations during T and therefore do not contribute to the oscillations.

When the phase of the blue spectral components of both beams E_a and E_b is shifted by π with the pulse shaping apparatus, the phase of the transient signal also shifts by π (green curve). Unlike the heterodyne detected transient grating measurement of diodomethane shown in Figure 4, in which the observed phase shift was due to a relative phase shift between the signal and LO beams, in the present case the phase shift of the homodyne detected signal in Figure 7 is due to quantum mechanical interferences between electronic coherences on the atoms that depend upon the spectral phases of the input fields.

A wide range of time–frequency domain experiments could be explored, such as multicolor multiple pulse experiments that would allow control over quantum pathways on the basis of pulse timing and spectral tuning. There are also interesting possibilities for purely frequency-domain measurements. A 2D measurement directly in the spectral domain is shown in Figure 8a. For this scan, fields E_a and E_c were time co-incident, not amplitude shaped, and covered all three spectral transitions within the laser bandwidth. The conjugate field, E_b , consisted of a narrow frequency component. The DFWM signal generated in this configuration was then measured with a spectrometer as a function of the center frequency of E_b , which was the scan parameter.

Many peaks are observed in the 2D DFWM spectrum of rubidium. The most prominent peaks, labeled A–D in Figure 8b, arise from diagrams R_5 – R_8 , as depicted in the appendix (Figure 17) and noted in Table 1. Peaks E and F in (b) arise from quantum pathways involving the state $|3\rangle$. The horizontally elongated peak shapes originate from the relatively large spectral width of the scanned frequency component within E_b .

There are also three weak peaks, G–I, observed in the 2D DFWM spectrum of rubidium that are not explainable with these third-order perturbation diagrams. A variety of higher-order nonlinear optical processes could give rise to these features. For instance, a degenerate fifth-order or cascaded third-order signals could be produced in the same direction as the signal. Due to the narrow absorption linewidths of rubidium, it is difficult to estimate the peak optical densities, based on which the higher-order signal strengths might be calculated. Additional experiments should be performed to determine the power dependence of these weak, unexpected peaks.

Unlike the 2D Fourier-transform measurements, which can take on the order of 1 h to record and which require involved procedures for data analysis, the present 2D spectrum was obtained in less than 1 min. The data acquisition time will be even faster once a recently acquired MEMS-based 2D SLM is used in place of the LC SLM. The MEMS device can operate

at repetition rates up to 330 Hz, whereas the LC SLM typically operates at 2–4 Hz. Further measurements and analysis should be performed to determine the connection between the novel 2D frequency-domain approach used above and the methods used in 2D Fourier-transform spectroscopy to obtain absorptive 2D spectra^{6,10,11,13,17} through addition of a measured 2D photon echo spectrum with a measured 2D transient grating spectrum. The absorptive spectrum is especially useful when the sought-after information is contained within the broad wings of the line shape or when the signs of the individual peaks within the 2D spectrum are desired.⁶

To determine the absorptive spectrum using our spectral scanning approach, the appropriate combination of transient grating (TG, diagrams R₅ and R₆) and photon echo (PE, diagrams R₇ and R₈) signals must be sampled. This may be easily achieved by shifting the spectrally broad pulses E_a and E_c in time such that neither overlaps temporally with the spectrally narrow pulse E_b . Then, to select the PE signal, E_a and E_c should follow E_b in time, or to select the TG signal, one of the pulses (for instance E_a) should precede E_b and the other pulse (E_c) should follow E_b . These measurements will require heterodyne detection to determine the absolute signs of the peaks, and phase cycling methods may be necessary to remove artifacts from the data (see phase-cycling discussion below). It may even be possible to use a double-pulse waveform within one of the beams, for instance E_a , such that one of the pulses arrives before E_b and the other arrives after E_b . Because E_c would still be timed to follow E_a , this pulse sequence would yield the absolute value 2D spectrum in a single experiment. A similar two-beam approach has been used for 2D infrared spectroscopy.³¹ Unlike that method, which relies upon two interactions between a spectrally narrow field and the sample followed by one interaction between the sample and a spectrally broad field, our approach still allows for independent manipulation of each interacting field. Polarization optics also could be incorporated in the paths of our separate input beams. Use of variably polarized input pulses has allowed for powerful simplifications of 2D infrared spectra.³²

C. Potassium Dimer. 1. Time-Integrated FWM Measurements. We next used our pulse-shaping based apparatus to perform two- and three-pulse FWM measurements on potassium dimer molecules. The potassium dimer vapor was contained within in a home-built heat pipe that was heated to 420 °C. The heat pipe was initially loaded with approximately 10 g of solid potassium within 100 mbar helium buffer gas. In the temperature range we used, the first approximately seven vibrational levels of the X state were populated (Figure 9a). With our laser center wavelength tuned to 815 nm, we were able to access the $v = 20$ –30 vibrational levels of the excited state. It was important to tune the center wavelength of the laser pulse away from the strong electronic resonances of atomic potassium vapor, at 766.5 and 769.9 nm, because the heat pipe contained large amounts of atomic potassium vapor but significantly smaller amounts of the dimer. A homodyne FWM measurement on potassium dimer is shown in Figure 9c for the pulse sequence illustrated in Figure 9b. An irregular signal is obtained (Figure 9c), with multiple peaks in the Fourier transformation shown in Figure 9d. The peak near 2 THz (as well as its harmonics) indicates excited state dynamics, and the peak near 3 THz indicates ground state dynamics, based on the vibrational frequencies, ω_e , of the two electronic states.

When a delay of 540 fs was introduced between pulses E_a and E_b , the FWM signal contained only a single frequency component (see Figure 10b) at the frequency 2.8 THz, corre-

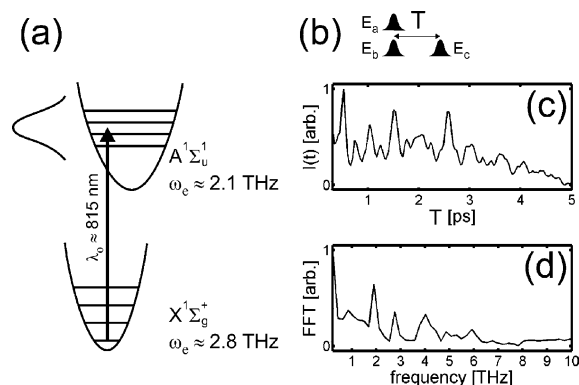


Figure 9. (a) Schematic illustration of relevant electronic energy levels for potassium dimer. (b) Pulse sequence. (c) Time-integrated FWM signal of potassium dimer with a complicated oscillatory structure. (d) Fourier transform of (c), indicating oscillatory contributions at integer multiples of the vibrational frequencies of the ground and excited electronic states.

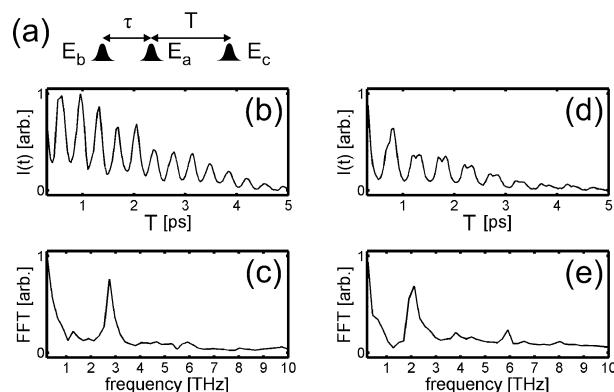


Figure 10. Pulse sequence (a) for time-integrated FWM measurement (b) of potassium dimer molecules, where the delay between the first two pulses was set to be 540 fs. Fourier transform of (b) showing ground state dynamics (c). When τ was set to be 720 fs, the resulting transient (d) oscillated at the excited state vibrational frequency (e).

sponding to the vibrational period of the ground electronic state (c). The delay 540 fs is slightly more than one vibrational period of the excited electronic state. When τ was set to 720 fs (slightly less than 1.5 times the excited state vibrational period), the observed transient (d) measured as a function of T showed oscillations with a frequency corresponding to the excited state vibrational frequency (e). Thus it is clear that the choice of pulse sequence is able to influence whether or not the measurement is sensitive to dynamics on the excited or the ground electronic surface. These effects arise from coherent vibrational oscillations in the excited electronic state wavepacket created by the first field. Depending on the delay between the first and second fields, the wavepacket may or may not be near to the Franck–Condon region where it was created and therefore may or may not be returned to the ground electronic state. The location of the wavepacket after the first two interactions determines whether the third field probes excited or ground state dynamics.^{33–35}

2. Field-Resolved FWM Measurements. The next step was to introduce a local oscillator beam that could be used to characterize the time-dependent emitted signal through spectral interferometry. Unfortunately, this step was not straightforward because we discovered that there were stray pulses within the pulse shaping apparatus itself that were obscuring our spectral interferometry measurements. Several careful cross-correlation

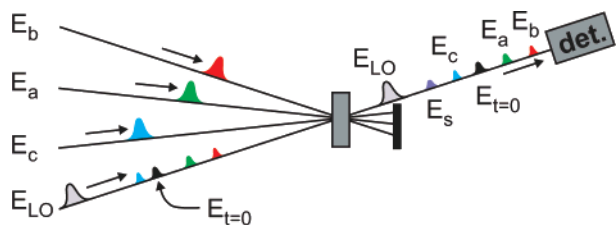


Figure 11. Schematic illustration of weak stray pulses in the direction of the LO pulse that distort the spectral interferometry measurements. Pulses a, b, and c are the three input fields that generate the outgoing signal S. In this case, the detector (det.) is a spectrometer.

measurements (not shown) revealed two types of stray pulses, as illustrated schematically in Figure 11. The first type of unwanted pulse results from very weak crosstalk between shaped regions E_a , E_b , E_c in the direction of the signal beam. These crosstalk pulses were most prominent for beams E_a and E_c , which neighbored the LO beam. Crosstalk from beam E_b was negligible, allowing us to use a reduced number of phase cycling steps, as discussed below. The second type of unwanted pulse occurs at time zero and may result from scattered zeroth-order light from the pulse shaper that is not properly blocked by the razor blades at the focal plane (see Figure 1). All of these stray pulses interfered within the spectrometer and obscured the desired signal. In general, these FWM signals are quite small, such that even weak stray pulses that are less than 1/1000 of the energy of the input pulses are still on order with or larger than the measured nonlinear signals. Because of this, we adapted phase cycling methods from multidimensional NMR to isolate the signal from the stray pulses obscuring the measurements. This approach, until now restricted to a collinear experimental geometry,¹² exploits the multiple-beam shaping capabilities that we have introduced.

In the case where there are no stray pulses, the intensity $I_{\text{det}}(\omega)$ recorded by the spectrometer is given by

$$I(\omega) \propto |E_{\text{LO}}(\omega) + E_s(\omega)|^2 \\ \approx A_{\text{LO}}(\omega)^2 + A_s(\omega)^2 + 2A_{\text{LO}}(\omega)A_s(\omega) \times \\ \cos[\phi_{\text{LO}}(\omega) - \phi_s(\omega)] \quad (3)$$

where $E(\omega) = A(\omega) \exp[i\phi(\omega)]$. When there are stray pulses, many additional cross terms will be produced (see eq 4), but none of them has the same phase dependence on the main three input pulses and local oscillator pulse as the desired cross term in eq 3.

$$I[\phi_{\text{LO}}(\omega), \phi_a(\omega), \phi_b(\omega), \phi_c(\omega)] \propto |A_{\text{LO}}(\omega) \times \\ \exp[i\phi_{\text{LO}}(\omega)] + A_s(\omega) \exp[i\phi_s(\omega)] + A_a(\omega) \times \\ \exp[i\phi_a(\omega)] + A_b(\omega) \exp[i\phi_b(\omega)] + A_c(\omega) \times \\ \exp[i\phi_c(\omega)] + A_{t=0}(\omega) \exp[i\phi_{t=0}(\omega)]|^2 \quad (4)$$

The basic approach is to perform multiple measurements with different input phases and to combine these results such that the unwanted terms disappear. This will be done in three steps that require a total of eight measurements. In the first step, all terms not dependent upon the phase of pulse E_a are eliminated. This is then repeated with two more measurements to eliminate all terms not dependent upon the phase of pulse E_b , and then four more measurements to eliminate all terms not dependent upon E_{LO} , which then isolates the term of interest. This set of eight measurements, in three stages, is written as

$$I_1(\phi_{\text{LO}}, \phi_a, \phi_b, \phi_c) = \\ I(\phi_{\text{LO}}, \phi_a + \pi, \phi_b, \phi_c) - I(\phi_{\text{LO}}, \phi_a, \phi_b, \phi_c) \\ I_2(\phi_{\text{LO}}, \phi_a, \phi_b, \phi_c) = \\ I_1(\phi_{\text{LO}}, \phi_a, \phi_b, \phi_c) - I_1(\phi_{\text{LO}}, \phi_a, \phi_b + \pi, \phi_c) \\ I_3(\phi_{\text{LO}}, \phi_a, \phi_b, \phi_c) = \\ I_2(\phi_{\text{LO}}, \phi_a, \phi_b, \phi_c) - I_2(\phi_{\text{LO}} + \pi, \phi_a, \phi_b, \phi_c) \quad (5)$$

The eight-step phase cycling procedure described in eq 5 yields the desired result:

$$I_3(\phi_{\text{LO}}, \phi_a, \phi_b, \phi_c) \propto A_{\text{LO}}A_s \cos[\phi_{\text{LO}} - \phi_a + \phi_b - \phi_c] \quad (6)$$

A simulation of such a phase-cycling process is shown in Figure 12. In the simulation, six pulses interfere to produce a complex interference pattern as a function of the delay of the LO beam. The relative amplitudes of E_{LO} , the crosstalk pulses, the time-zero pulse, and the signal, respectively, were chosen to be 100, 5, 5, and 1. The arrival times of the crosstalk pulses from E_b , E_a , E_c and the signal pulse E_s were set to -0.75 , $+0.25$, $+0.75$, and $+1.25$ ps, respectively, whereas E_{LO} was scanned in time. The first plot, (a), shows a series of spectral interferograms as a function of the delay of E_{LO} . A complicated set of interference fringes is observed. After each phase-cycling stage, the unwanted signal contributions diminish. Finally in (d), eight measurements have been combined, yielding the expected pattern for a signal field emitted at a time of 1.25 ps that interferes with a variably delayed reference pulse. The fringe spacing (along the vertical dimension) is inversely proportional to the temporal separation of the two pulses that interfere. When the two pulses overlap, the fringes disappear, leaving a single broad fringeless spectrum, as can be seen for a LO delay of 1.25 ps. In experiments, it is not necessary to scan the LO pulse in time, although we have found the LO delay scans to be useful when investigating the effects of the unwanted pulses due to cross talk, etc. A single spectral interferogram^{36,37} recorded for a given LO delay can provide all the necessary information to characterize the emitted signal field because, upon dispersion in the spectrometer, the separated frequency components of the signal and LO fields overlap temporally and interfere to yield the desired information. Eight cycles are sufficient to isolate the third-order nonlinear optical signal from the spurious pulses, provided that each of the spurious pulses is only dependent upon the phase of a single input pulse. Related phase cycling schemes can in principle be used to discriminate between nonlinear signals of a different order (e.g., to separate fifth-order responses from third-order responses).

Figure 13 shows two stages of the phase cycling process used in preliminary experiments. For the photon-echo pulse sequence shown in (a), the time-integrated signal in (b) was obtained as a function of T , with τ held constant at 0.54 ps. An arrow in (b) points to a specific peak in the time-integrated signal ($T = 1$ ps), which we investigated with several phase-cycled LO scans. The LO scan shown in (c) has already been through the first step of the phase cycling process (two combined measurements). There are broad features centered at a time of about 1.5 ps, the position at which the echo signal is expected, as well as smaller features that originate from the $t = 0$ pulse. Repeating the phase cycling operation performed in (c) (a single phase cycle) with one of the noncycled phases flipped by π causes the interference fringes to flip in sign, as can be seen in (d). The difference between (c) and (d) is plotted in (e), where the smaller features originating from $t = 0$ have been eliminated

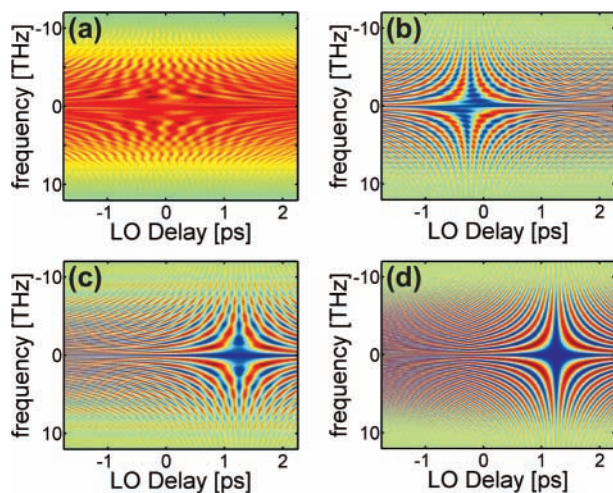


Figure 12. Simulation of LO scans, illustrating how phase-cycling can be used to eliminate spurious signals that are not dependent on the phase of all beams. (a) Original interferogram, no phase cycles. (b) Two phase cycles. (c) Four phase cycles. (d) Eight phase cycles, yielding the correct signal free of distortions.

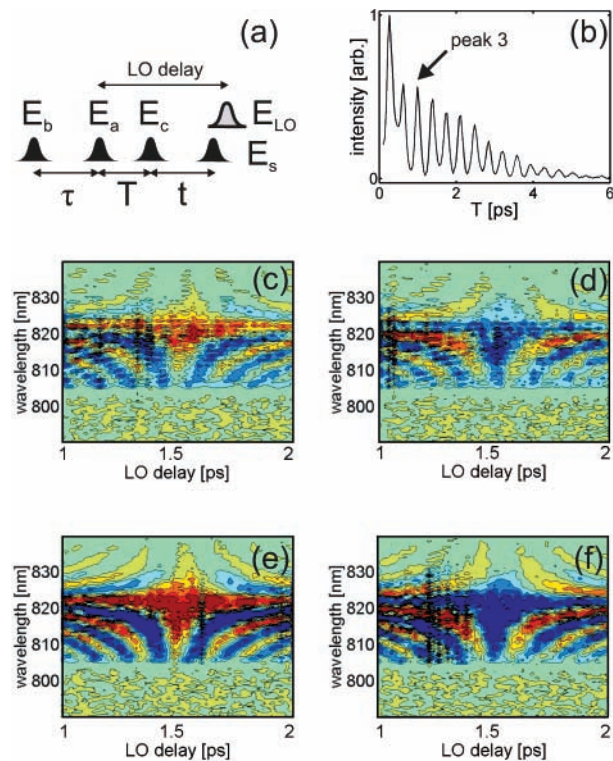


Figure 13. (a) Photon echo pulse sequence. For $\tau = 0.54$ ps, T is scanned in time, yielding the transient in (b). For a fixed value of $T = 1$ ps [see arrow in (b)], LO scans were recorded for varying amounts of phase-cycling (c)–(f). Spurious high-frequency interferences that are evident upon close inspection of (b) are eliminated through phase cycling.

and the expected interference pattern is much clearer. Thus, (e) constitutes a spectrum that has been through two stages of the phase cycling process (four measurements). When the measurement in (e) is repeated but with one of the noncycled phases flipped by π , the sign of the interference fringes is switched. The difference between (e) and (f) would then constitute the full three stages of phase cycling (total of eight measurements). This step was not necessary though, because the crosstalk of beam E_c into E_{LO} was negligible.

A second set of LO scans is shown in Figure 14, where this time, $T = 1.3$ ps [which, again, corresponds to a peak in the

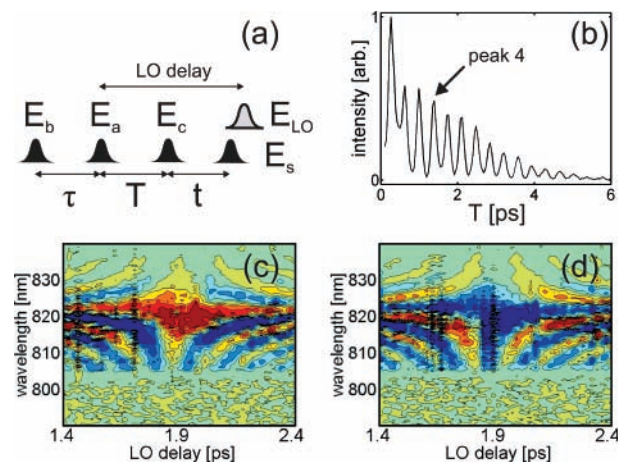


Figure 14. (a) Photon-echo pulse sequence. For $\tau = 0.54$ ps, T is scanned in time, yielding the transient in (b). When T is set to be 1.3 ps [see arrow], the observed phase-cycled signal shifts to the expected time of about 1.85 ps (c), (d). Two sets of phase cycling (four measurements) were used in each of (c) and (d). Note that dark vertical lines are artifacts due to unusually large laser fluctuations.

time-integrated signal (b)]. As expected, the peak of the echo signal has shifted in time to about 1.85 ps (c), (d). We again performed measurements where the phase of one of the pulses not involved in the phase cycling scheme was shifted by π , and as expected, the photon echo also showed this additional phase shift. It is worth noting that the fringes observed in Figures 13 and 14 do not have an overall tilt to them, as they would if mechanical or refractive delay lines were used, because these delay methods shift both carrier phase and envelope. Because 800 nm light has a period of about 2.7 fs, there would be about 370 tightly spaced fringes running diagonally across the 1 ps LO scans of Figure 13 and 14. By using the pulse shaper to shift the envelope of the pulse without shifting the phase, it is not necessary to resolve oscillations of the carrier phase. The ability to use rotating frame detection, adapted from NMR, applies for 2D measurements generally, not just the LO scan as illustrated here. For each temporal variable that is scanned, appropriate phase cycling has to be performed to eliminate the effect of the crosstalk pulses on the heterodyned signal.

D. 2D Spectra of GaAs/AlGaAs Quantum Wells. Although the systems discussed above serve well as test beds for the development of new experimental methodology, ultimately we wish to turn our attention to more complex molecules and materials. In this section we show 2D FT spectra from GaAs/AlGaAs multiple quantum wells whose interactions and dynamics still pose unresolved problems that are pertinent to semiconductor laser physics and a fundamental understanding of many-body interactions. Transient four-wave-mixing studies of semiconductors, unlike those of atoms, show signal at negative delays,^{38,39} a classic signature of many-particle correlations that are to be expected even at low densities of excitons due to the long-range Coulomb interaction. The aim has been to understand the microscopic mechanisms and consequences of this interaction. These include excitation-induced dephasing⁴² and excitation-induced spectral shift,^{43,44} which are understood as renormalization of the exciton dephasing rate and energy, respectively, due to interactions between each exciton and the fluctuating local field arising from all the excitons around it. The formation of four-particle correlations between excitons of opposite spin, or biexcitons,^{40,41} also contributes to the signal. Recent 2D FWM measurements on GaAs/AlGaAs^{15,45,46} exhibit separate features that result from the specific microscopic many-body interaction

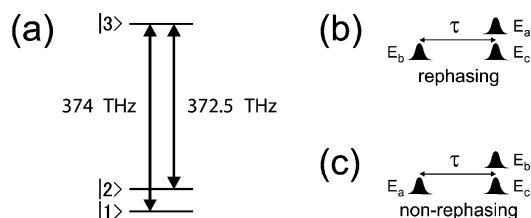


Figure 15. (a) Energy level diagram for the GaAs/AlGaAs quantum well structure. Rephasing (b) and non-rephasing (c) pulse sequences, where E_b is the conjugate field.

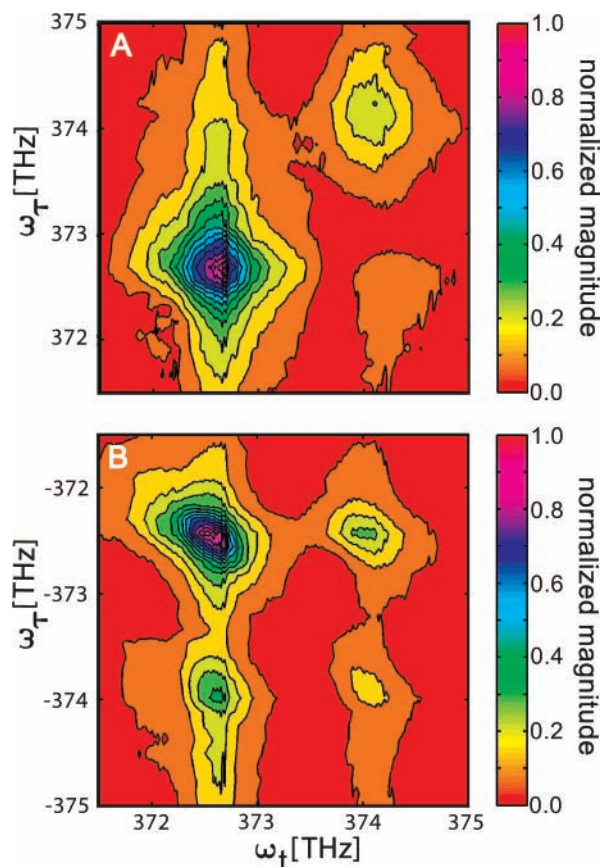


Figure 16. Magnitude of the 2D Fourier transform for nonrephasing (a) and rephasing (b) pulse sequences for GaAs/AlGaAs quantum wells which highlight the electronic coupling between the light hole and heavy hole excitons.

mechanisms discussed above. In those measurements, actively stabilized interferometers were used to maintain phase stability among multiple input fields. In our experiments reported here, we have begun applying the spatiotemporal waveform shaping approach to the study of exciton dynamics in quantum well structures.

The sample contains 10 layers of 10 nm thick GaAs, separated by 10 nm thick barriers of $\text{Al}_{0.3}\text{Ga}_{0.7}\text{As}$. Quantum confinement splits the degeneracy of the valence band into what is termed the heavy hole and light hole bands. They couple through the conduction band to form a three-level single particle energy level system (see Figure 15), with resonances at 372.5 and 374 THz, respectively. (Higher-lying biexciton levels are not shown.) In the experiments reported in this section, each of the three excitation pulses had an energy of 0.2 pJ, whereas the LO pulse had an energy of 0.2 fJ. We estimate the carrier density to be 10^{10} carriers/cm²/well. The sample was cooled to ~ 10 K in a coldfinger cryostat. The signal was heterodyne detected and spectrally dispersed along the dimension ω_t for all values of the delay τ . Four-step phase cycling was used, which was

sufficient in this case to eliminate the largest contributors of scattered light and extract a clean signal. In two separate measurements, the conjugate field, E_b and the non-conjugate field, E_a , were scanned over the time range 0 to -4 ps in 15 fs steps. The mixing time, T , was zero. The spectral fringes created between the signal and LO fields were analyzed as described earlier³⁶ to extract the full signal amplitude and phase information. The resulting 2D spectra for the nonrephasing and rephasing pulse sequences are shown in Figure 16a,b, respectively. Here, we use the term nonrephasing to denote a pulse sequence where a nonconjugate field arrives first at the sample (virtual echo) and the term rephasing to denote a pulse sequence where the conjugate field arrives first (photon echo).⁴⁷

The results appear to be closely consistent with those reported earlier.^{15,45,46} The off-diagonal features in the amplitude spectra arise from coupling between light and heavy hole excitons, and the vertical stripes at the heavy hole emission frequency represent excitation of the continuum (unbound electron–hole) states. Further experimentation is under way to examine biexciton coherences, exploiting the optical coherence among all four beams that is generally not maintained when separate diffractive optics are used to generate pairs of beams or when beamsplitters and a limited number of interferometric phase-locked loops are employed.

IV. Conclusions

A new approach to coherent nonlinear optical spectroscopy, including coherent multidimensional spectroscopy, has been proposed and demonstrated. The use of automated 2D phase and amplitude pulse shaping allows generation of multiple, noncollinear, fully phase coherent input fields with facile control over the wavevectors, pulse timings and phases, spectral content, and features of more complex waveforms that may include multiple pulses, chirped pulses, etc. Any of these parameters may be used as a basis for selection of nonlinear spectroscopic signals, and may be scanned in the collection of data. Thus a subset of possible measurements includes coherent multidimensional spectroscopy conducted entirely in the frequency domain, in mixed time–frequency domains, or entirely in the time domain. Phase cycling for enhanced signal selectivity and carrier-free interferometric detection for determination of the full signal field were demonstrated.

In many respects, spatiotemporal phase/amplitude shaped spectroscopy integrates key elements of multidimensional NMR spectroscopy, including complex waveform generation, phase cycling, and rotating frame signal collection, into multidimensional nonlinear optical spectroscopy without compromising the wavevector-based signal selectivity of the latter. The absence of active optical elements besides the spatiotemporal pulse shaper and the need for few optical elements altogether, as well as the interferometric stability inherent in the common-path optical apparatus, permit extremely robust operation that should be possible in nonideal environments including commercial instruments outside a laser laboratory. Extensions of the approach will enable greatly enhanced selectivity of signals in higher than third-order nonlinear spectroscopy.

Acknowledgment. We thank the X. Li and S. T. Cundiff for providing the quantum well sample and for assistance with these measurements. We also thank M. F. DeCamp for helpful discussions. This research received support in part from National Science Foundation grant number CHE-0212375. T.H. gratefully acknowledges the Deutsche Forschungsgemeinschaft for financial support (“Forschungsstipendium”).

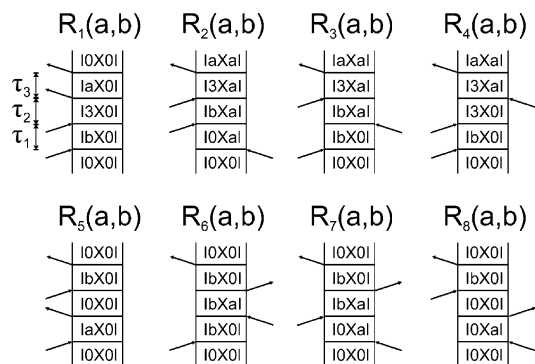


Figure 17. Feynman diagrams for Rb invoking the rotating wave approximation and assuming a signal detection in the direction $\vec{k}_s = \vec{k}_a - \vec{k}_b + \vec{k}_c$. The ket (bra) vectors $|a\rangle$ and $|b\rangle$ stand for either level $|1\rangle$ or $|2\rangle$ ($\langle 1|$ or $\langle 2|$). Thus each $R_i(a,b)$ stands for four specified diagrams, leading to a total of 32 diagrams.

V. Appendix

In the Rb frequency domain experiments, described in section IIIB of this paper, 40 fs pulses in direction \vec{k}_a and \vec{k}_c contain the full spectrum and are time co-incident. The pulse in direction \vec{k}_b is amplitude shaped to contain only a single frequency that is scanned. As a consequence this pulse is long in duration. Because the pulses from all three directions thus overlap in time, no time ordering can be specified. It follows then, invoking the rotating wave approximation for the four-level system of rubidium (see Figure 6), and assuming noncollinear detection in the direction $\vec{k}_s = \vec{k}_a - \vec{k}_b + \vec{k}_c$, that the set of Feynman diagrams shown in Figure 17 contributes to the measured signal. Note that each of these eight diagrams contains four subdiagrams, because the ket (bra) vector $|a\rangle$ and $|b\rangle$ can stand for either level $|1\rangle$ or $|2\rangle$ ($\langle 1|$ or $\langle 2|$). In total $8 \times 4 = 32$ diagrams contribute to the third-order Rb signal in the detection direction $\vec{k}_s = \vec{k}_a - \vec{k}_b + \vec{k}_c$. The number of diagrams can be further reduced, if one notes that in the experiments described in the paper, the $|1\rangle \rightarrow |3\rangle$ transition could not be excited by the laser pulses, because there was no spectral amplitude at 761 nm. Thus instead of four subdiagrams only the subdiagrams with $a = 1$ as part of the diagrams $R_1(a,b)$, $R_2(a,b)$, $R_3(a,b)$, and $R_4(a,b)$ contribute to the signal. This reduces to the total number of diagrams to $4 \times 2 + 4 \times 4 = 24$. Depending on the wavelength of the pulse in direction b (the scan parameter) and the observed signal wavelength, one can assign the diagrams for each peak observed in the two-dimensional ω_s versus ω_b data plot of Figure 8. See Table 1 in section IIIB for the detailed assignment.

References and Notes

- (1) Ernst, R. R.; Bodenhausen, G.; Wokaun, A. *Principles of Nuclear Magnetic Resonance in One and Two Dimensions*; Oxford University Press: Oxford, U.K., 1987.
- (2) Hamm, P.; Lim, M.; DeGrado, W. F.; Hochstrasser, R. M. *Proc. Natl. Acad. Sci., U.S.A.* **1999**, *96*, 2036–2041.
- (3) Zhao, W.; Wright, J. C. *Phys. Rev. Lett.* **2000**, *84*, 1411–1414.
- (4) Golonzka, O.; Khalil, M.; Demirdoven, N.; Tokmakoff, A. *Phys. Rev. Lett.* **2001**, *86*, 2154–2157.
- (5) Woutersen, S.; Mu, Y. G.; Stock, G.; Hamm, P. *Proc. Natl. Acad. Sci., U.S.A.* **2001**, *98*, 11254–11258.
- (6) Khalil, M.; Demirdoven, N.; Tokmakoff, A. *J. Phys. Chem. A* **2003**, *107*, 5258–5279.
- (7) Fulmer, E. C.; Ding, F.; Zanni, M. T. *J. Chem. Phys.* **2005**, *122*, 034302.

- (8) Cowan, M. L.; Bruner, B. D.; Huse, N.; Dwyer, J. R.; Chugh, B.; Nibbering, E. T. J.; Elsassner, T.; Miller, R. J. D. *Nature* **2005**, *434*, 199–202.
- (9) Zheng, J. R.; Kwah, K.; Asbury, J.; Chen, X.; Piletic, I. R.; Fayer, M. D. *Science* **2005**, *309*, 1338–1343.
- (10) Hybl, J. D.; Ferro, A. A.; Jonas, D. M. *J. Chem. Phys.* **2001**, *115*, 6606–6622.
- (11) Jonas, D. M. *Annu. Rev. Phys. Chem.* **2003**, *54*, 425–463.
- (12) Tian, P. F.; Keusters, D.; Suzuki, Y.; Warren, W. S. *Science* **2003**, *300*, 1553–1555.
- (13) Cowan, M. L.; Ogilvie, J. P.; Miller, R. J. D. *Chem. Phys. Lett.* **2004**, *386*, 184–189.
- (14) Brixner, T.; Stenger, J.; Vaswani, H. M.; Cho, M.; Blankenship, R. E.; Fleming, G. R. *Nature* **2005**, *434*, 625–628.
- (15) Zhang, T.; Borca, C. N.; Li, X.; Cundiff, S. T. *Opt. Express* **2005**, *13*, 7432–7441.
- (16) Maznev, A. A.; Nelson, K. A.; Rogers, J. A. *Opt. Lett.* **1998**, *23*, 1319–1321.
- (17) Brixner, T.; Mancal, T.; Stiopkin, I. V.; Fleming, G. R. *J. Chem. Phys.* **2004**, *121*, 4221–4236.
- (18) Feurer, T.; Vaughan, J. C.; Koehl, R.; Nelson, K. A. *Opt. Lett.* **2002**, *27*, 652–654.
- (19) Vaughan, J. C.; Feurer, T.; Nelson, K. A. *Opt. Lett.* **2003**, *28*, 2408–2410.
- (20) Vaughan, J. C.; Hornung, T.; Feurer, T.; Nelson, K. A. *Opt. Lett.* **2005**, *30*, 323–325.
- (21) Vaughan, J. C.; Feurer, T.; Hornung, T.; Nelson, K. A. Manuscript in preparation.
- (22) Hornung, T.; Vaughan, J. C.; Feurer, T.; Nelson, K. A. *Opt. Lett.* **2004**, *29*, 2052–2054.
- (23) Weiner, A. M. *Rev. Sci. Instrum.* **2000**, *71*, 1929–1969.
- (24) Vaughan, J. C.; Feurer, T.; Stone, K. W.; Nelson, K. A. *Opt. Express* **2006**, *14*, 1314–1328.
- (25) Yan, Y. X.; Nelson, K. A. *J. Chem. Phys.* **1987**, *87*, 6240–6256.
- (26) Nelson, K. A.; Ippen, E. P. *Adv. Chem. Phys.* **1989**, *75*, 1–35.
- (27) Goodno, G. D.; Dadusc, G.; Miller, R. J. D. *J. Opt. Soc. Am. B* **1998**, *15*, 1791–1794.
- (28) Mukamel, S. *Principles of Nonlinear Optical Spectroscopy*; Oxford University Press: Oxford, U.K., 1995.
- (29) Weiner, A. M.; Leaird, D. E.; Wiederrecht, G. P.; Nelson, K. A. *Science* **1990**, *247*, 1317–1319.
- (30) Blank, D. A.; Kaufman, L. J.; Fleming, G. R. *J. Chem. Phys.* **1999**, *111*, 3105–3114.
- (31) Cervetto, V.; Hebling, J.; Bredenbeck, J.; Hamm, P. *J. Chem. Phys.* **2004**, *121*, 5935–5942.
- (32) Zanni, M. T.; Ge, N. H.; Kim, Y. S.; Hochstrasser, R. M. *Proc. Nat. Acad. Sci., U.S.A.* **2001**, *98*, 11265.
- (33) Brown, E. J.; Pastirk, I.; Grimberg, B. I.; Lozovoy, V. V.; Dantus, M. *J. Chem. Phys.* **1999**, *111*, 3779–3782.
- (34) Hornung, T.; Meier, R.; Motzkus, M. *Chem. Phys. Lett.* **2000**, *326*, 445–453.
- (35) Dantus, M.; Lozovoy, V. V. *Chem. Rev.* **2004**, *104*, 1813–1859.
- (36) Lepetit, L.; Cheriaux, G.; Joffre, M. *J. Opt. Soc. Am. B* **1995**, *12*, 2467–2474.
- (37) *J. Opt. Soc. Am. B* **2000**, *17*, 1795–1802.
- (38) Leo, K.; Wegener, M.; Shah, J.; Chemla, D. S.; Gobel, E. O.; Damen, T. C.; Schmitt-Rink, S.; Schafer, W. *Phys. Rev. Lett.* **1990**, *65*, 1340–1343.
- (39) Wegener, M.; Chemla, D. S.; Schmittring, S.; Schafer, W. *Phys. Rev. A* **1990**, *42*, 5675–5683.
- (40) Bott, K.; Heller, O.; Bennhardt, D.; Cundiff, S. T.; Thomas, P.; Mayer, E. J.; Smith, G. O.; Eccleston, R.; Kuhl, J.; Ploog, K. *Phys. Rev. B* **1993**, *48*, 17418–17426.
- (41) Albrecht, T. F.; Bott, K.; Meier, T.; Schulze, A.; Koch, M.; Cundiff, S. T.; Feldmann, J.; Stolz, W.; Koch, S. W.; Gobel, E. O. *Phys. Rev. B* **1996**, *54*, 4436–4439.
- (42) Shacklette, J. M.; Cundiff, S. T. *Phys. Rev. B* **2002**, *66*, 045309.
- (43) Shacklette, J. M.; Cundiff, S. T. *J. Opt. Soc. Am. B* **2003**, *20*, 764–769.
- (44) Wang, W. L.; Ferrio, K.; Steel, D. G.; Hu, Y. Z.; Binder, R.; Koch, S. W. *Phys. Rev. Lett.* **1993**, *71*, 1261–1264.
- (45) Borca, C. N.; Zhang, T.; Li, X.; Cundiff, S. T. *Chem. Phys. Lett.* **2005**, *416*, 311–315.
- (46) Li, X.; Zhang, T.; Borca, C.; Cundiff, S. T. *Phys. Rev. Lett.* **2006**, *96*, 057406.
- (47) Mukamel, S. *Annu. Rev. Phys. Chem.* **2000**, *51*, 691–729.